Nano Energy 59 (2019) 443–452

Contents lists available at ScienceDirect

Nano Energy

journal homepage: www.elsevier.com/locate/nanoen

Full paper

Synergistic effect of charge transfer and short H-bonding on nanocatalyst surface for efficient oxygen evolution reaction

Jinlong Yang[a,1], Yinguo Xiao[a,1], Qinghe Zhao[a], Guangxing Zhang[a], Rui Wang[a], Gaogeng Teng[a], Xin Chen[a], Mouyi Weng[a], Daping He[b], Shichun Mu[b], Yuan Lin[a], Feng Pan[a,*]

[a] School of Advanced Materials, Peking University, Shenzhen Graduate School, Shenzhen 518055, People's Republic of China
[b] State Key Laboratory of Advanced Technology for Materials Synthesis and Processing, Wuhan University of Technology, Wuhan 430070, People's Republic of China

ARTICLE INFO

Keywords:
Water splitting
Oxygen evolution reaction
Nanocatalyst
Synergistic effect
Short H-bonding

ABSTRACT

Exploring advanced electrocatalysts with unprecedented catalytic efficiency for oxygen evolution reaction (OER) of water splitting is of great importance in many energy conversion and storage systems. Based on our previous findings that short H-bonding on reconstructed β_{II}-Li_2CoSiO_4 (LCS) nanocrystal surface to enhance OER activity by facilitating proton transfer/dissociation and an electronic push/pull effect of Co and Fe doping on OER performance of Ni-based hydroxides, here we report both combination of Fe-Co synergistic effect with charge transfer and short H-bonding on $Li_2Co_xFe_{1-x}SiO_4$ ($LC_xF_{1-x}S$, $0 < x < 1$) nanocatalyst surface can further enhance OER performances of water splitting. Especially, $LiC_{0.5}F_{0.5}S$ exhibits superior OER activity and super-long term stability (no fade after 10,000 CV cycles, high temperature of 80 °C, and 100 h OER measurement at a low overpotential of 0.3 V with high current density of 80 mA cm^{-2}). Insight of the ultrahigh OER performance of $LC_{0.5}F_{0.5}S$ is suggested to attribute to the short H-bonding formed on the constructed surface and the synergistic coupling effect between Fe and Co with charge transfer, which leads to favorable electronic structure of TM active sites, promotes proton out of the oxygen on Co site and generates H_2O on Fe site by proton transfer.

1. Introduction

Exploring advanced nanocatalysts with unprecedented catalytic efficiency is key to enhance the performance of many energy conversion and storage systems. The sluggish oxygen evolution reaction (OER) at the anode has long been the major bottleneck hindering the improvement of energy conversion efficiency of water splitting to produce hydrogen, regenerative fuel cells and rechargeable metal-air batteries [1–4]. High performance OER catalysts are required to lower the overpotential, accelerate the kinetics and sustain the catalytic stability. To substitute the state-of-the-art but expensive and scarce Ir, Ru-based OER catalysts [5,6], inexpensive and earth-abundant transition-metal (TM = Fe, Co, Ni, Mn, Mo, V, W, etc.) alternatives such as oxide [7–9], hydroxide [10–12], sulfides [13–15], selenides [16], phosphides [17–19], nitrides [20] and borides [21] have been explored with promising advances, especially in alkaline solution. However, the current catalyst materials are still far from meeting the requirements of combined high catalytic activity, long-term stability, and low cost. New strategies to develop efficient OER catalysts are still desirable.

It has been disclosed that TM ions on the surface of TM-based OER catalysts are the main active sites, which electrostatically interact with nearby molecules (including reactants, intermediates and products) in an electrochemical potential [22]. The electronic structures and coordination environments tightly control the catalytic activity of TM active site through adjusting the adsorption/desorption of the molecules involved in OER [23]. Liu and Co-workers demonstrated that the OER activity of Co^{2+} ion in the tetrahedral site was considerably higher than that of Co^{3+} ion in the octahedral site [24]. Recently, we firstly designed and fabricated β_{II}-typical lithium cobalt silicate (β_{II}-LCS) nanocrystal to outperform the state-of-the-art IrO_2 and the previously reported Co-based catalysts due to the line-linked arrangement of Co active sites at the surface of β_{II}-LCS, short H-bonding (2.54 Å) are formed and linked into a network at the reconstructed surface by rotating the flexible CoO_4 tetrahedra after surface delithiation, thus to facilitate proton transfer and dissociation, leading to a unique dual-center catalytic pathway with low theoretical thermodynamic overpotential (0.35 eV) for the OER process [25].

In addition, numerous studies confirm that the formation of multimetallic structures represents a common strategy to improve OER performance of electrocatalysts, especially the incorporation of Fe often

* Corresponding author.
E-mail address: panfeng@pkusz.edu.cn (F. Pan).
[1] These authors contributed equally to this work.

https://doi.org/10.1016/j.nanoen.2019.02.053
Received 23 August 2018; Received in revised form 23 January 2019; Accepted 19 February 2019
Available online 20 February 2019

remarkably boost catalytic activity [26–32]. Based on the extensive literature investigation, it has been understood that there is a great difference in the mechanism of iron to boost catalytic activity in different material systems. For example, our previous work revealed that a Fe dopant pulls partial electrons from nearby Ni/Co active sites resulting in a higher electron affinity at the Ni/Co sites to facilitate OH^- adsorption and charge transfer from the adsorbed OH^- for OER [33]. Fominykh et al. [29] reported that 10%Fe-doped NiO decreased the particle size of nanocrystals and increased the surface Ni atoms that are involved in the electrochemical reaction. Trotochaud et al. [26] demonstrated that Fe in β-$Ni_{1-x}Fe_xOOH$ not only exerted a partial-charge transfer activation effect on Ni, but also showed a > 30-fold increase in film conductivity. Friebel et al. [30] found that Fe^{3+} cations in γ-$Ni_{1-x}Fe_xOOH$ exhibit a significantly lower overpotential than that of Ni^{3+} cations in either γ-$Ni_{1-x}Fe_xOOH$ or γ-NiOOH. Burke et al. [27] found that FeOOH is an insulator with conductivity of 2.2×10^{-2} mS cm^{-1} at high overpotentials larger than 400 mV and its OER activity is limited by low conductivity, and thus hypothesized that Fe is the most-active site in the $Co_{1-x}Fe_xOOH$ catalyst, while CoOOH primarily provides a conductive, high-surface area, chemically stabilizing host. Zhu et al. [32] indicated that the dramatically enhanced performance of $LiCo_{0.8}Fe_{0.2}O_2$ is attributed to increased number of highly oxidative oxygen species O_2^{2-}, better charge transfer ability, and greater O_2 desorption capability. However, what effect does Fe incorporation have on the full-tetrahedral structure and all Co^{2+} active sites of β_{II}-LCS? What about their electrocatalytic properties? To clarify these questions, the Fe-incorporated β_{II}-LCS catalyst need to be synthesized and investigated, which would serve as guidelines for us to explore advanced nanocatalysts with unprecedented catalytic efficiency.

Herein, we designed and fabricated novel hollow lithium cobalt-iron silicate ($Li_2Co_xFe_{1-x}SiO_4$, $0 \le x \le 1$, named as $LC_xF_{1-x}S$) hierarchical nanostructures, engineered cobalt-iron ratios by using a facile hydrothermal route, and investigated the roles of Fe and Co, charge transfer between Co and Fe, and short H-bonding on reconstructed surfaces to facilitate proton transfer as dual-center catalytic pathway with their composition-dependent activity for electrochemical OER in alkaline solution. Among them, $LC_{0.5}F_{0.5}S$ with 50% Fe incorporation is proved to be the best OER catalyst with ~8-fold higher in mass activity (MA), ~20-fold higher in specific activity (SA) and ~140-fold higher in turnover frequency (TOF) compared with that of pure LCS. Moreover, $LC_{0.5}F_{0.5}S$ exhibits super stability since there is no fade after 10,000 CV cycles or 100 h OER measurements at overpotential of 0.3 V. When the $LC_{0.5}F_{0.5}S$ is tested at an optimum temperature of 75 °C, the overpotential decreases to 0.190 V, which is almost the best catalysts that has ever been reported. Experimental results show that the ultrahigh OER performance of $LC_{0.5}F_{0.5}S$ not only benefits from the short H-bonds formed on the constructed surface but also from the synergistic coupling effect between Fe and Co with charge transfer, which leads to favorable electronic structure of TM active sites, promotes proton out of the oxygen on Co site and generates H_2O on Fe site by proton transfer.

2. Results and discussion

2.1. Preparation and characterization of $LC_xF_{1-x}S$ ($0 \le x \le 1$) nanocatalysts

A series of $LC_xF_{1-x}S$ ($0 \le x \le 1$) materials were synthesized by a facile hydrothermal method (Detail are seen in Section 4). Various cobalt-iron composites can be facilely prepared by adjusting the cobalt-iron precursor salts. First, the actual molar ratios of Co/Fe in samples (Table S1) were determined by inductively coupled plasma atomic emission spectrometry (ICP-AES), which are very close to the source ratio. Then, the as-synthesized $LC_xF_{1-x}S$ ($0 \le x \le 1$) samples were characterized by field-emission scanning electron microscopy (FESEM). Fig. 1a–c show that LCS, $LC_{0.5}F_{0.5}S$ and LFS exhibit the high quality of the homogeneous and freestanding 3D assembly with average diameter of ~300 nm. Moreover, each particles show open voids, indicating the formation of hollow structures. Higher magnification images in inset of Fig. 1a–c show that all 3D structures are woven by small particles, forming a networked cage-like structure. A deeper observation further reveals that the shapes of LCS and LFS are almost spherical but $LC_{0.5}F_{0.5}S$ presents a square structure. X-ray powder diffraction (XRD) were used to identify the crystal structure evolution of the $LC_xF_{1-x}S$ ($0 \le x \le 1$) upon Fe substitution. As demonstrated in series of XRD patterns (Fig. 1d), the crystal structure of samples are significantly changed with increasing Fe concentration. Although both LCS and LFS crystallize in orthorhombic structure with a $Pmn2_1$ space group, their crystal structures are different due to different atomic site occupancy [25,34]. In LCS, half of Li atoms occupy 2*a* site and half of Li atoms share 4*b* site with Co atoms, while all Li atoms occupy 4*b* site and Fe atoms occupy 2*a* site in LFS. Indeed, the crystal structure of both LCS and LFS are composed of TMO_4 (TM = Fe, Co), LiO_4 and SiO_4 tetrahedra in different arrangement, as illustrated in Fig. S1. Based on XRD patterns, the Rietveld profile fitting technique was used to refine the crystal structure of LCS, LFS and $LC_{0.5}F_{0.5}S$ samples (Figs. S2–4), and the refinement results are presented in Table S2–4 in SI, including the lattice parameters, atomic coordinates and reliability factors. It is clear that $LC_{0.75}F_{0.25}S$ maintains the crystal structure as LCS, while the crystal structures of $LC_{1-x}F_xS$ samples with Fe content ≥50% exhibit similar structure as LFS. The phase boundary can be determined roughly based on the peak shift of (002) reflection, as demonstrated in Fig. 1e. The similar (002) peak position of the samples with ≤50% Fe incorporation further confirms that $LC_{0.5}F_{0.5}S$ adopted same crystal structure as that of LCS. Our previous study [25] has demonstrated that the $Pmn2_1$-LCS structure is an excellent OER electrocatalysts.

The microstructure of $LC_{0.5}F_{0.5}S$ is further investigated by transmission electron microscopy (TEM). Fig. 1f confirms the hollow structure with a shell composed of nanocrystals with dozens of nanometers in length and width. The corresponding selected area electron diffraction (SAED) patterns (inset of Fig. 1f) confirmed the single-crystal nature of the majority of nanocrystals, and the labeled diffraction spots are consistent with the crystal surfaces of (0-11), (1-10), (2-1-1), (10-1) and (01-1) in orthorhombic structural $LC_{0.5}F_{0.5}S$. Fig. 1g shows that the lattice fringe with spacing of 0.364 nm is indexed to the (011) facet of $LC_{0.5}F_{0.5}S$. The energy-dispersive X-ray (EDX) elemental mapping images of Co, Fe, O, and Si are displayed in Fig. 1h–k, indicating the uniformity of the element distribution in a single assembly with hollow structure. These results demonstrate that $LC_{0.5}F_{0.5}S$ adopts the full tetrahedral structure, within all tetrahedral point in the same direction, perpendicular to the close-packed planes, and CoO_4/FeO_4 tetrahedra link into several active lines along the a-axis direction by vertex oxygen (Inset of Fig. 1d).

2.2. Electrocatalytic performances of $LC_xF_{1-x}S$ ($0 \le x \le 1$) nanocatalysts Overpotential for OER

The OER electrocatalytic performances of a series of $LC_xF_{1-x}S$ ($0 \le x \le 1$)were investigated in alkaline solution (1 M KOH) by using a standard three-electrode setup with a loading of 0.2 mg cm^{-2}. All of the potentials were calibrated against the reversible hydrogen electrode (RHE) for comparison. It is well known that the performance of catalysts can be affected by deposition substrate [13,35]. Firstly, we selected Ni foam and carbon nanotube (CNT) paper as the substrates, respectively. Obviously, the OER performances of catalysts coated on Ni foam is better than that of catalysts coated on CNT paper (Fig. S5). There are three possible reasons: i) the conductivity and electron transfer ability of Ni substrate are better than that of carbon substrate [13]; ii) Ni foam itself is a good catalyst for OER (Fig. S6); iii) the reported Ni-Co and Ni-Fe bimetallic catalysts [36,37] confirm that Ni has a synergistic effect with other transition metals. Therefore, Ni substrate affects the determination of the composition-depended electrocatalysis performances and CNT paper is selected in this work.

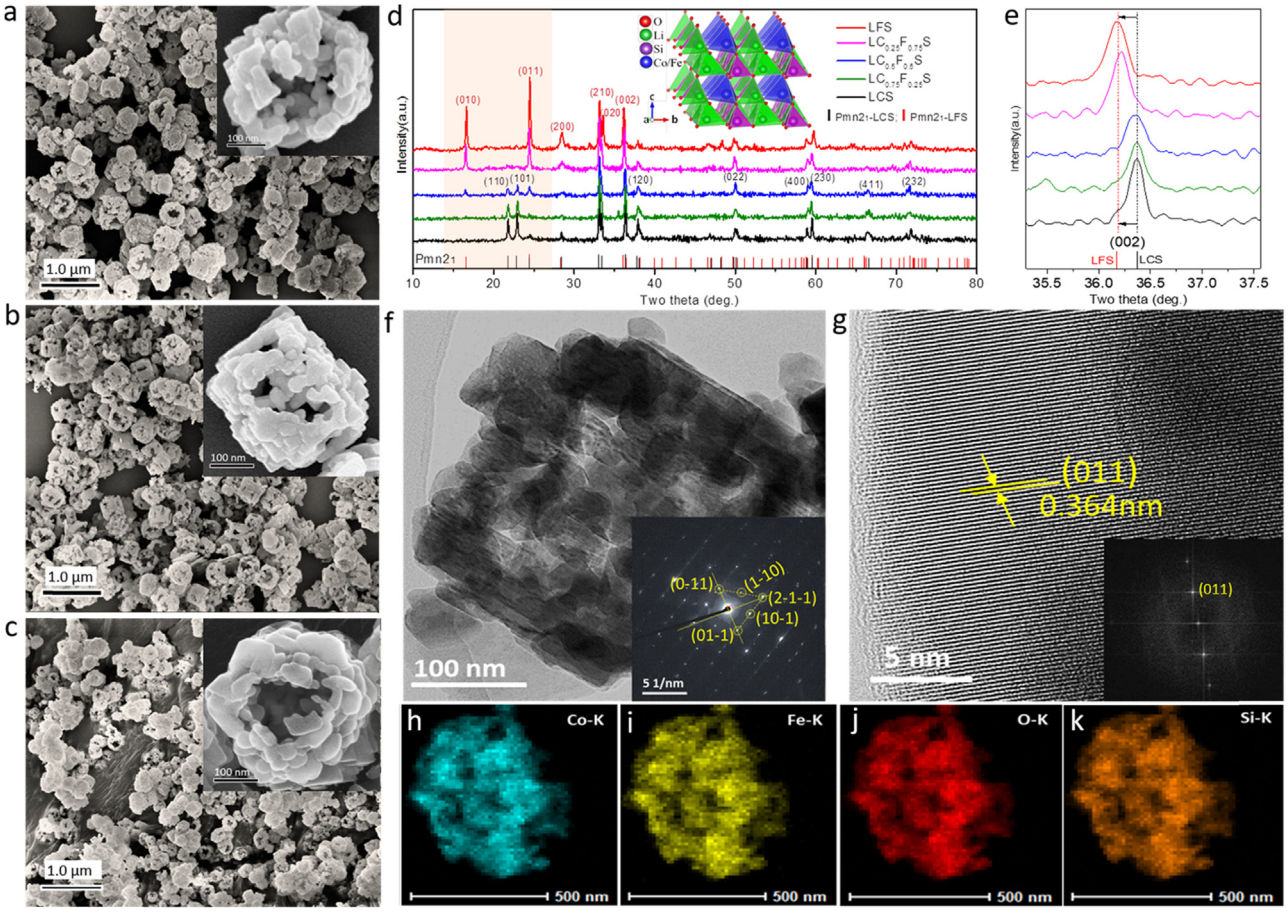

Fig. 1. Morphologies and structures of as-obtained $LC_xF_{1-x}S$ ($0 \le x \le 1$) samples. SEM images of (a) LCS, (b) $LC_{0.5}F_{0.5}S$ and (c) LFS, (d) XRD of $LC_xF_{1-x}S$, inset of (d) is schematic presentation of $LC_{0.5}F_{0.5}S$ with full tetrahedral structure, (e) (002) peak of $LC_xF_{1-x}S$, (f) TEM and (g) HRTEM, and (h-i) EDX elemental mapping images of $LC_{0.5}F_{0.5}S$, inset of (f) and (g) are the corresponding SAED pattern and FFT pattern, respectively.

Fig. 2a shows the polarization LSV curves of $LC_xF_{1-x}S$ ($0 \le x \le 1$) coated on CNT paper with different amounts of Fe. The onset potential of $LC_{0.5}F_{0.5}S$ is 1.42 V, which is 60 mV lower than that of pure LCS (1.48 V). Pure LFS is almost inactive at this potential. Besides the value of onset potential, the overpotential at 10 mA cm^{-2} (η_{10}) is another key parameter for OER performance evaluation. Fig. 2b shows that the η_{10} follows the order: $LC_{0.5}F_{0.5}S$ (0.23 V) < $LC_{0.75}F_{0.25}S$ (0.25 V) < $LC_{0.25}F_{0.75}S$ (0.27 V) < LCS (0.30 V) < LFS (0.45 V). Remarkably, the η_{10} of all Fe incorporation of $LC_xF_{1-x}S$ ($0 < x < 1$) are smaller than the best values reported in IrO_2 (0.33 V)[6] and RuO_2 (0.30 V) [5]. Moreover, The OER current density depended on the Fe content in a volcano-like fashion (Fig. 2b), the current density of $LC_{0.5}F_{0.5}S$ rises much faster than that of the other Fe-contained catalysts. Specifically, at the overpotential of 0.3 V, the current density of $LC_{0.5}F_{0.5}S$ is even 8-fold and more than 150-fold higher than that of LCS and LFS, respectively.

2.3. Kinetics for OER

The Tafel plots of the catalysts are further investigated to get additional insight into their OER performance. According to the Tafel equation ($\eta = b*\log j + a$), the Tafel slope (b) defines overpotential (η) depended on the current density (j) in the Tafel region, and a small Tafel slope corresponds to rapid reaction kinetics, thus leading to high OER activity. As can be seen in Fig. 2c, the Tafel slopes fellow the order: $LC_{0.5}F_{0.5}S$ (38 mV dec^{-1}) < $LC_{0.75}F_{0.25}S$ (45 mV dec^{-1}) < $LC_{0.25}F_{0.75}S$ (49 mV dec^{-1}) < LCS (57 mV dec^{-1}) < LFS (106 mV dec^{-1}). Among them, the Tafel slope of pure LFS (106 mV dec^{-1}) is closed to theoretical value of 120 mV dec^{-1}, suggesting that the adsorption of reacts is the main rate-determining step [38]. The Tafel slopes of pure LCS and partial Fe incorporation $LC_xF_{1-x}S$ ($0 < x < 1$) are more close to theoretical value of 30 mV dec^{-1}, indicating that the proton dissociation along with O-H bond breaking is the main rate-determining step [25]. In addition, charge transfer resistances were obtained by electrochemical impedance spectroscopy (EIS) measurements (Fig. S7). The charge transfer resistance (Rct) of $LC_{0.5}F_{0.5}S$ (0.4 Ω) was smaller than that of other $LC_xF_{1-x}S$ (0.8 Ω), LCS (2.5 Ω) and LFS (24 Ω). As results, the minimum Tafel slope and Rct values of $LC_{0.5}F_{0.5}S$ confirms that 50% Fe incorporation promotes the proton dissociation and leads to the fastest kinetics. Based on the small overpotential and fast kinetics, the mass activity (MA $= j/c$, where j is the current density at a given overpotential, c is the loading (0.2 mg cm^{-2}) of catalysts on carbon paper) of the best $LC_{0.5}F_{0.5}S$ at the overpotential of 0.3 V can reach 400 A g^{-1}, which is 40 and 160-fold higher than that of pure LCS and LFS, respectively (Fig. 2d).

2.4. Intrinsic activity

To gain insights into the intrinsic activity of the catalysts, we measured the double-layer capacitances (C_{dl}) to calculate the electrocatalytic active surface areas (ECSAs) and further normalized the geometric current density to the corresponding ECSA to estimate the specific activity (SA = j/ECSA) (Fig. S8). It can be observed from Fig. 2e that the ECSAs of pure LCS, $LC_{0.5}F_{0.5}S$ and $LC_{0.75}F_{0.25}S$ are not very different, but when the ratio of Fe incorporation further increases, their ECSAs exhibit slipping dramatically from 166 mF cm^{-2} ($LC_{0.5}F_{0.5}S$) to 50 mF cm^{-2} ($LC_{0.25}F_{0.75}S$), indicating over 50% Fe incorporation is not

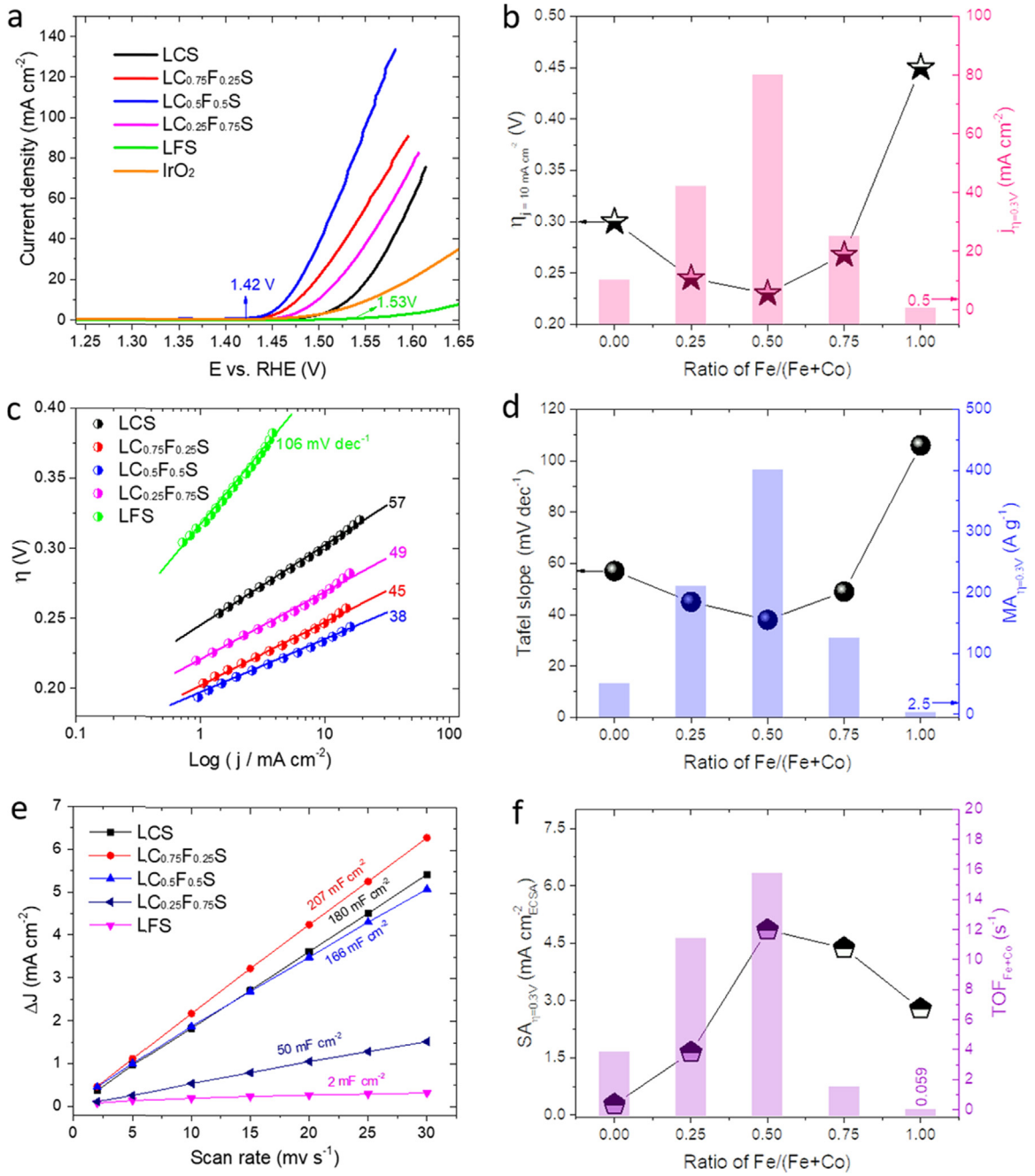

Fig. 2. Electrocatalytic activities of $LC_xF_{1-x}S$ ($0 \le x \le 1$) samples for OER. (a) Polarization LSV curves at 1.0 mV s^{-1} in 1 M KOH electrolyte, (b) comparison of overpotential at current density of 10 mA cm^{-2} and current density at overpotential of 0.3 V, (c) Tafel plots, (d) comparison of Tafel slope and mass activity at overpotential of 0.3 V, (e) charging current density differences (ΔJ = Ja-Jc) plotted versus scan rate. The linear slope, equivalent to twice the double-layer capacitance C_{dl}, was used to represent the ECSA, (f) comparison of specific activity and TOF at overpotential of 0.3 V.

favorable to expose active sites. Fig. 2f shows the SA values at overpotential of 0.3 V vs. the ratio of Fe incorporation in catalysts. The $LC_{0.5}F_{0.5}S$ exhibits the largest SA values, which is 20-fold larger than that of pure LCS, indicating 50% Fe incorporation is intrinsically more active than pure catalyst. We also calculated the O_2 turn over frequencies (TOFs) by assuming that all the metal sites (both Co and Fe) in the catalysts are active to evaluate the intrinsic OER activity. Particularly, the TOF is as high as16.4 s^{-1} associated with the $LC_{0.5}F_{0.5}S$ at an overpotential of 0.3 V (Fig. 2f). This value is much higher than those of $LC_{0.75}F_{0.25}S$ (2.92 s^{-1}), $LC_{0.25}F_{0.75}S$ (4.63 s^{-1}), LCS (0.12 s^{-1}) and LFS (0.06 s^{-1}). These observations confirmed that the Fe incorporation enhanced the intrinsic activity of the catalysts.

2.5. Durability and temperature effect of $LC_{0.5}F_{0.5}S$ nanocatalyst

The long-term durability of OER catalyst is essential for practical applications. Fig. 3a shows that the OER polarization curve of $LC_{0.5}F_{0.5}S$ after 1000 and ultralong 10,000 potential cycles almost overlaps with the original one. Moreover, we carried out Chronoamperometry measurement (j-t) on the $LC_{0.5}F_{0.5}S$ catalyst under constant overpotential of 0.3 V continuously for 100 h. Although the current density is up to a very high level of 80 mA cm^{-2}, we observed no appreciable increase in potential in this time interval (Fig. 3b). In addition, $LC_{0.5}F_{0.5}S$ can well maintain its hollow hierarchical nanostructure during long-time OER processes (Fig. S9). These results demonstrate that the $LC_{0.5}F_{0.5}S$ possesses a long-term durability for efficient oxygen evolution

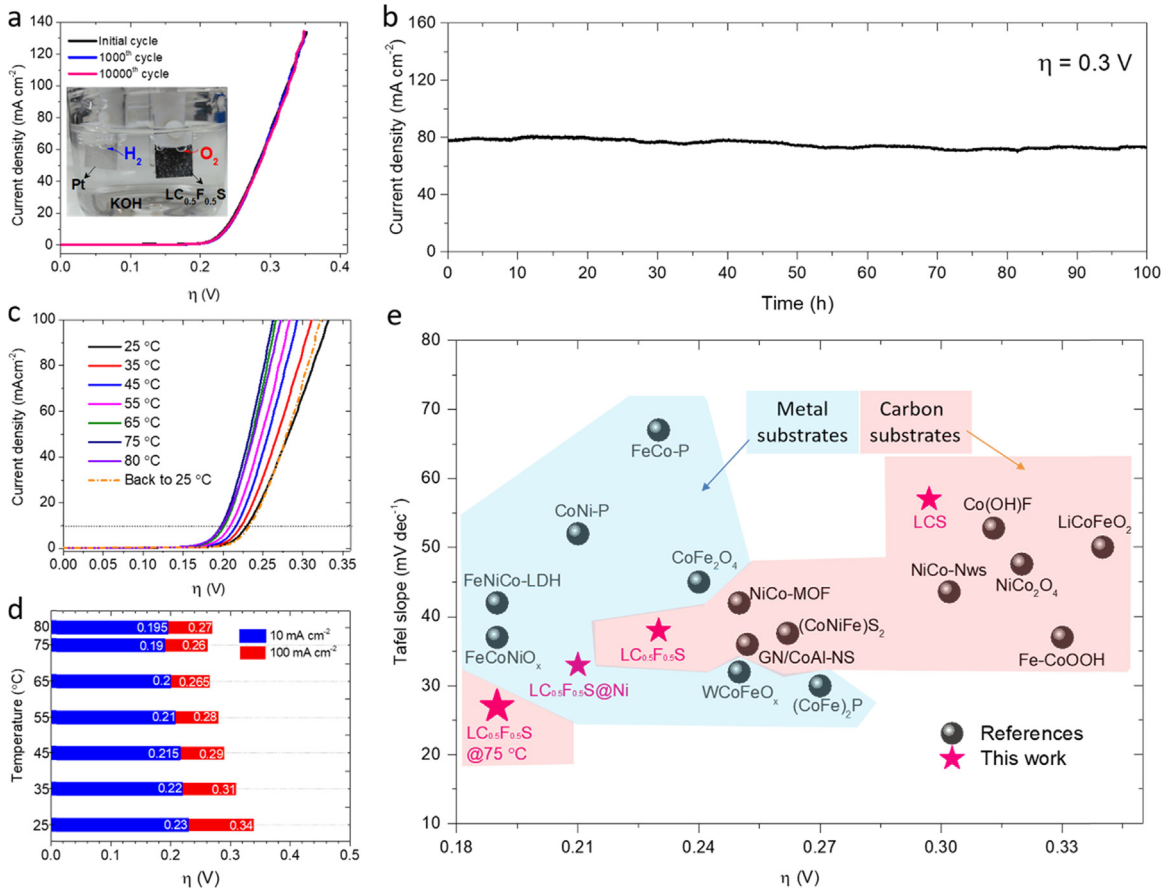

Fig. 3. Long-term durability and temperature effect of the $LC_{0.5}F_{0.5}S$ sample for OER. (a) Polarization LSV curves with initial, 1000 and 10,000 cycles at 2 mV s^{-1}, (b) chronoamperometric response at η = 0.3 V, (c) polarization LSV curves from 25 to 80 °C at 2 mV s^{-1}, (d) comparison of overpotential at current densities of 10 and 100 mA cm^{-2} with different temperatures, (e) OER activity comparison graph showing overpotential at 10 mA cm^{-2} and Tafel slopes, with references (Table S5 in SI) all measured in 1 M KOH.

electrocatalysis.

In addition, we also investigated the temperature effect and the stability at high temperature, which was found some Co-contained catalyzers [39]. Fig. 3c shows the LSV cures of $LC_{0.5}F_{0.5}S$ tested at temperature between 25 °C and 80 °C. It can be seen that the OER overpotential and current density of $LC_{0.5}F_{0.5}S$ disobey the traditional Arrhenius' law ($k = A \exp(-E_a/RT)$, where k is reaction rate, A is constant, T is temperature, and E_a is the activation energy.) and follow the temperature variation regularity of Co-based catalysts [39]. The Arrhenius' law suggests that the higher temperature, the faster reaction rate so that one can obtain a larger OER current density at a lower η by raising the temperature. However, at a moderate temperature of 75 °C, the overpotentials of $LC_{0.5}F_{0.5}S$ at 10 and 100 mA cm^{-2} are the minimal 0.19 and 0.26 V, respectively, and increased overpotential with increasing temperature (Fig. 3d). Moreover, once the temperature is decreased to 25 °C from high temperature of 80 °C, the LSV cures was closed to that at initial 25 °C (Fig. 3c), which verifies the stability after high temperature. This temperature regulation and stability are valuable to guide the practical application of water splitting and rechargeable metal air batteries.

Fig. 3e shows a comparison for the catalytic activity (η_{10}) and kinetics (Tafel slopes) of the $LC_xF_{1-x}S$ series with previously reported multi-metal OER electrocatalysts (detailed values in Table S5 in SI). It is clear that the η_{10} of catalysts on metal substrate (red region) are lower than that of one on carbon substrate (blue region). More importantly, the η_{10} of $LC_{0.5}F_{0.5}S$ on the same substrate, no matter it's metal or carbon, is much smaller than that of the reported excellent bimetallic catalysts. Meanwhile, the $LC_{0.5}F_{0.5}S$ at moderate temperature of 75 °C can reach the minimum η_{10} value reported currently and along with improvement of kinetics (Tafel slope < 30 mV dec^{-1}).

2.6. Deep understanding of OER mechanisms

The insight of original outstanding OER performance of $LC_{0.5}F_{0.5}S$ are further investigated from roles of cobalt-iron synergistic effects and forming types of hydrogen bond on the reconstructed surface. X-ray photoelectron spectroscopy (XPS) provided a direct evidence of cobalt-iron synergistic effect. In initial $LC_{0.5}F_{0.5}S$ catalyst, the Co2p binding energies (Fig. 4a) exhibited a 0.5 eV shift to higher values compared with LCS (780.8 and 797.0 eV are respectively corresponding to Co2p3/2 and Co2p1/2 of Co^{2+} [25]), indicating a modified local electronic structure of $Co^{(2-\delta)+}$ (δ is likely close to 0, the standard 2p3/2 binding energy of Co^{3+} is 779.5 eV [25]). Meanwhile, the binding energy of Fe2p3/2 (710.8 eV) and Fe2p1/2 (724.5 eV) in pure LFS (Fig. 4b) is corresponding to Fe^{2+} [40]. 0.6 eV higher binding energies of Fe2p in $LC_{0.5}F_{0.5}S$ demonstrated that a part of electron of Fe given to adjacent Co and the Fe is a slightly higher $Fe^{(2+\delta)+}$ (δ is likely close to 0, the standard 2p3/2 binding energy of Fe^{3+} with tetrahedral coordination is 712.6 eV [41]). Moreover, a similar deviation appeared in the XPS spectra (Fig. S10) of samples after OER. It can be concluded that the active sites of Co and Fe in $LC_{0.5}F_{0.5}S$ samples are synergistic. Furthermore, the cobalt-iron synergistic effect was also observed on the electrochemical curves. We compared the CV cures of $LC_xF_{1-x}S$ ($0 \le x \le 1$) with different Fe content. Fig. 4c shows that the $Co^{2+/3+}$ wave shifts anodically as the Fe content in $LC_xF_{1-x}S$ catalyst increases, indicating a strong electronic interaction between the Co and Fe that

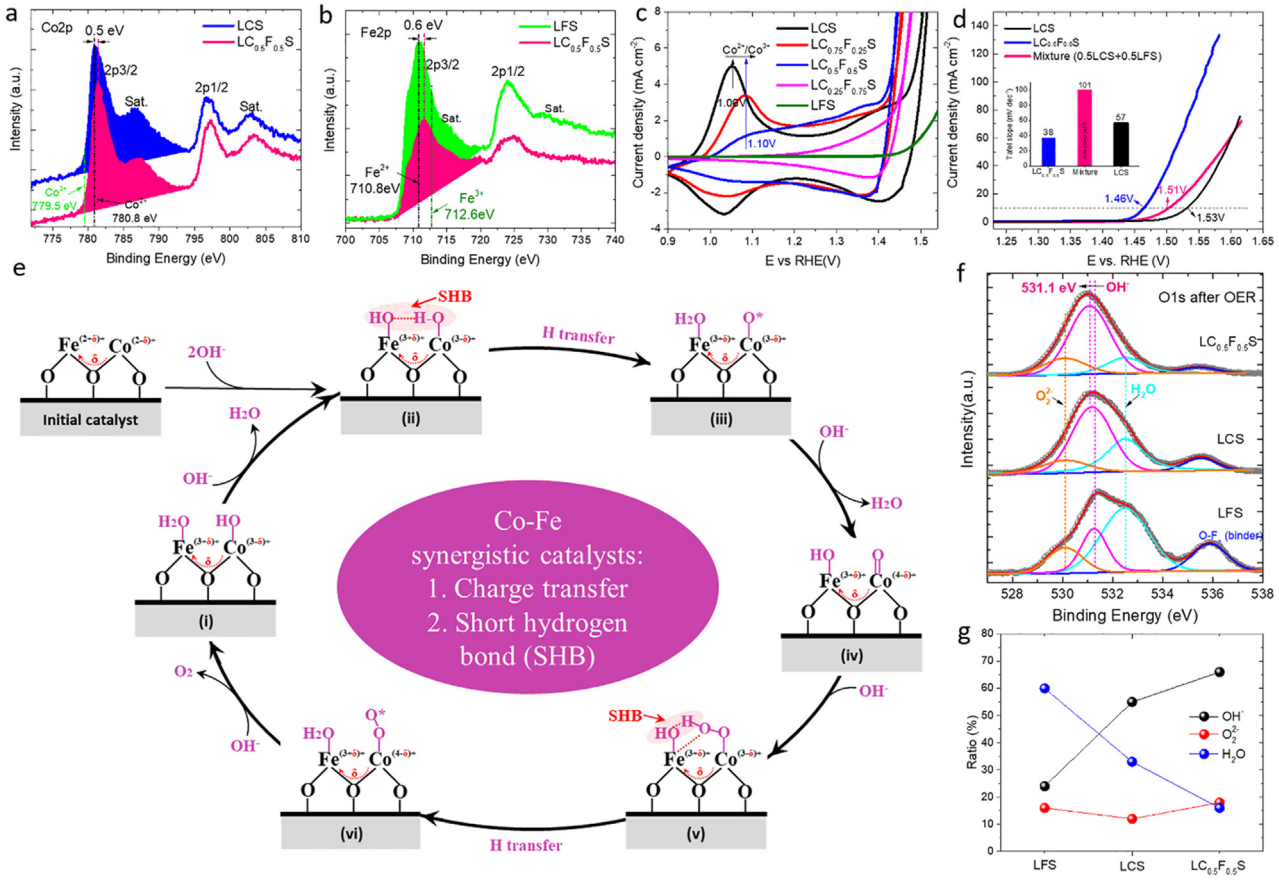

Fig. 4. Cobalt-iron synergistic effect on OER electrocatalytic activity. (a) Co2p and (b) Fe2p binding energies of the initial LCS, LFS and $LC_{0.5}F_{0.5}S$ catalysts, (c) Co^{2+}/Co^{3+} redox peaks in CV curves at 10 mV s^{-1}, (d) OER performance comparison of $LC_{0.5}F_{0.5}S$, LCS and physical mixing of LFS and LCS, (e) proposed OER reaction pathway with cobalt-iron synergistic catalysts, (f) O1s spectra and (g) the ratios of OH^-, O_2^{2-} and H_2O in catalysts after OER.

modifies the electronic structure of the catalyst thus making Co^{2+} oxidation more difficult and conversely electron accepting of Co active sites much easier. In addition, three LSV cures of $LC_{0.5}F_{0.5}S$, LCS and physical mixing of LFS and LCS at a low scan rate of 1.0 mV s^{-1} are shown in Fig. 4d. The mixture has the same quantity of elements as $LC_{0.5}F_{0.5}S$, but its whole curve shift anodically and current density rises gently, exhibiting higher overpotential and larger Tafel slope (101 mV dec^{-1}). Meanwhile, comparing with the pure LCS, the η_{10} (1.51 V) of mixture is lower but its current density at high potential (> 1.6 V) is more poor. The negative results indicate that performance improvement of $LC_{0.5}F_{0.5}S$ is not due to simple confounding but synergistic effect.

A proposed OER reaction pathway for the overall transformation is shown in Fig. 4d using the cobalt-iron synergistic model derived from experimental studies. The OER activity is strongly dependent on the structure of initial catalyst. In an alkaline solution, the molecules involved in OER are mainly water (H_2O) and hydroxide (OH^-). As the voltage increases, Co and Fe active sites are oxidized and the negatively charged OH^- gradually migrates to the surface of the catalyst and form the adsorption structure (ii). Noteworthily, we had proved in our previous work on LCS [25] that the high electrocatalytic OER performance of transition-metal silicate material benefited from its all-tetrahedral structure with point connection, which helped to form short H-bonds (2.54 Å) on the reconstructed surface by rotating of the flexible tetrahedra and facilitate proton transfer and dissociation, leading to a possible dual-center catalytic pathway with low theoretical thermodynamic energy barrier (0.35 eV) for OER. In that work, we have already used both negatively shift of O-H stretching peak in FTIR and O1s binding energy corresponded to OH^-, as well as theoretical calculations to show that the short H-bonding is formed on the reconstructed surface of LCS catalyst. As shown in Fig. 4e, the OH^- binding energies of LCS and $LC_{0.5}F_{0.5}S$ catalysts, except that of LFS, shift negatively to 531.1 eV, which corresponded to the characteristics of the short H-bonding and facilitated proton (H) transfer between two TM active sites during OER. However, comparing with Co^{3+} site in pure LCS, the $Co^{(3-\delta)+}$ site in $LC_{0.5}F_{0.5}S$ is easier to get electron and promotes proton out of the oxygen. On the contrary, the $Fe^{(3+\delta)+}$ benefits oxygen to combine proton and generate H_2O on this site, so intermediate (iii) formed spontaneously after H transfer. The intermediate (iv) is obtained after the H_2O dissociation and OH^- resorption on Fe site along with further oxidation of Co site, in which OH^- in electrolyte quickly links to the Co = O bond. Benefiting from the strong adsorption of Fe site, the intermediate (v) with short H-bonding emerges and then turns to intermediate (vi). The O1s binding energies corresponded to O_2^{2-} (530.1 eV) [32,42] and H_2O (532.5 eV) [25,32] provided a strong evidence of the existence of the adsorption structure (vi). Especially, the fitted results from subpeaks area of the oxygen species (Fig. 4f) show a high ratio of O_2^{2-} (16%) and H_2O (60%) on the surface of inactive LFS, indicating an overly stable intermediate on the surface hinders the further absorption of OH^- and the release of O_2. However, high ratio of OH^- demonstrates that LCS (55%) and $LC_{0.5}F_{0.5}S$ (66%) can smoothly return to adsorption structure (i) and (ii). Furthermore, based on our previous caculated method of LCS catalysts [25], we found Fe-Co synergistic LCFS catalyst possesses shorter SHB (2.47 Å) to cause spontaneous H transfer (energies on all site between Co and Fe are < 0 eV) and facilitate easier H dissociation (energy barrier of 0.02 eV) during OER process (Fig. S11). Therefore, we concluded that the ultrahigh OER performance of $LC_{0.5}F_{0.5}S$ is attributed to the Co-Fe synergy with charge

transfer to promote the formation of short H-bond, proton transfer and dissociation.

3. Conclusions

we have reported a series of novel $LC_xF_{1-x}S$ ($0 \le x \le 1$) hierarchical nanostructures as electrocatalysts for OER in alkaline solution. We have found that the optimum OER catalyst, $LiC_{0.5}F_{0.5}S$ with 50% Fe incorporation, exhibits ~40-fold higher in mass activity (MA), ~20-fold higher in specific activity (SA) and ~140-fold higher in turnover frequency (TOF) than pure LCS, together with super stability (no decay after 10,000 CV cycles and 100 h OER measurements with 80 mA cm^{-2} at $\eta = 0.3$ V). We have further observed that the overpotential of $LC_{0.5}F_{0.5}S$ at 10 mA cm^{-2} (η_{10}) decreases to 0.190 V when tested at an optimum temperature of 75 ℃, which is almost beyond the best catalysts that has been reported. We have further demonstrated that the ultrahigh OER performance not only benefits from the formation of short H-bonding but also from unusual synergistic coupling effects between Co and Fe with charge transfer, which promotes proton out of the oxygen on Co site and H_2O generated on Fe site by proton transfer.

4. Experimental procedures

4.1. Synthesis of $LC_xF_{1-x}S$ ($0 \le x \le 1$) nanocatalysts

A series of $LC_xF_{1-x}S$ ($0 \le x \le 1$) materials were synthesized by a facile hydrothermal method. Typically, LiOH (0.1 mol, Aldrich) was gradually added to 40 mL of ethanol solution with TEOS (0.025 mol, Aldrich) and stirred for 30 min to form a homogeneous and white solution. Then, A certain stoichiometric ratio of $CoSO_4$ (Aldrich) and $FeSO_4$ (Aldrich) were added to 40 mL of ethylene glycol and stirred until dissolution occurred. For example, 0.0125 mol of $CoSO_4$ and 0.0125 mol of $FeSO_4$ for $LC_{0.5}F_{0.5}S$. The two solutions were then mixed by stirring, and the slurry was transferred to a 100 mL Teflon-lined autoclave. The above mixture was next placed into an autoclave and heated at 180 ℃ for 12 h. After the autoclave was cooled to room temperature, the obtained products were centrifuged at 10,000 rpm and washed with deionized water and ethanol several times. Finally, the product was dried in a vacuum oven (80 ℃, 12 h) for subsequent use.

4.2. Characterizations

The crystal structures of the samples were characterized via X-ray diffraction (XRD, Bruker D8 Advance diffractometer with Cu Kα). Rietveld refinements were performed using the TOPAS 4.2 package. The morphologies and size of the samples were observed via field emission scanning electron microscopy (FE-SEM, ZEISS Supra 55). The microstructures were investigated by transmission electron microscopy and selected area electron diffraction (SAED) (TEM, Tecnai G2 F20 S-TWIN, 200 kV). The element distribution was exhibited by energy-dispersive X-ray (EDX) mapping. The binding energy of element was analyzed by X-ray photoelectron spectroscopy (XPS) using a Thermo Fisher ESCALAB 250X.

4.3. Electrochemical testing

Electrochemical measurements were conducted in a three-electrode setup with a Ag/AgCl (PINE, sad. KCl) as the reference electrode and a Pt coil as the counter electrode, the preparation of working electrode is as follow: In brief, 10 mg of catalyst powder was dispersed in 2 mL of 3:1 v/v water/isopropyl alcohol mixed solvent with 90 μL of Nafion solution (5 wt%, Sigma-Aldrich). The mixture was then ultrasonicated for about 1.0 h to generate a homogeneous ink. Next, 40 μL of the dispersion was transferred onto CNT films or Ni foams (1.0 cm * 1.0 cm), leading to a catalyst loading of ~0.2 mg cm^{-2}. The electrolyte was 1 M KOH aqueous solution (99.99% metal purity, pH ~13.6). The potentials were celibrated against and converted to the reversible hydrogen electrode (RHE), where $E_{(RHE)} = E_{(Ag/AgCl)} + 0.998$ V. The cell was purged with O_2 for 30 min prior to each set of experiments. The work electrode first undergo a cyclic voltammetry (CV) activation of 50 cycles at 100 mV s^{-1}. After that, all linear sweep voltammetry (LSV) were carried out at 2.0 mV s^{-1}. All the potentials were 75% internal resistance (iR) corrected unless noted (The contact resistance are shown in Fig. S7). The long-term stability was evaluated by chronoamperometry, the chronoamperometry curves of the catalysts were collected at a constant overpotential of 0.3 V.

The mass activity (MA, A g^{-1}) were calculated from the catalyst loading mass (m = 0.2 mg cm^{-2}) and the measured current density j (mA cm^{-2}) at $\eta = 0.3$ V by the following Eq. (1) [16,32]:

$$MA = \frac{\mathbf{j}}{\mathbf{m}} \tag{1}$$

The electrochemical capacitance (C_{dl}) was determined from cyclic voltammograms (which are shown in Fig. S8) measured in a non-Faradaic region at different scan rates (v), the double-layer current (i) is equal to the product of the v. The C_{dl} is then calculated according to the Eq. (2) [36,43]:

$$Cdl = \frac{\delta(\Delta i(0.25\text{V vs. Ag/AgCl}))}{\delta(v)} \tag{2}$$

The electrochemically active surface area (ECSA) was estimated from the electrochemical double-layer capacitance according to the following Eq. (3) [43,44]:

$$ECSA = \frac{\mathbf{C}dl}{\mathbf{C}cnt} \tag{3}$$

where C*cnt* is a C_{dl} value of CNT substrate in 1.0 M KOH.

The specific activity (SA, mA cm^{-2}) were calculated from ECSA (m^2 g^{-1}), catalyst loading mass (m = 0.2 mg cm^{-2}), and the tested current density (j, mA cm^{-2}) at $\eta = 0.3$ V [44,45]:

$$SA = \frac{j}{\text{m*ECSA}} \tag{4}$$

The TOF values were calculated by assuming that every metal atom (Fe + Co) is involved in the catalysis (lower TOF limits were calculated) [27,46]:

$$TOF = \frac{j\text{*ECSA}}{4*F*n} \tag{5}$$

here, the number 4 reflects four electrons per mole of O_2, F is the Faraday constant (96,485.3 C mol^{-1}), and n is the moles of the metal atom on the electrode calculated from the mass and the molecular weight of the coated catalysts.

Author contributions

J. Y. and Y. X. contributed equally to this investigation. J. Y. and Y. X. designed the project and performed the catalyst preparation and tests. Q. Z., G. Z., R. W., and G. T. carried out measurements and data analyses. X. C and M. W. performed the ab inito calculations. D. H., S. M., Y. L., and F. P. discussed the results, analyzed the data, and drafted the manuscript. All authors reviewed the manuscript.

Acknowledgments

The research was financially supported by National Natural Science Foundation of China (No. 51602009), China Postdoctoral Science Foundation (2016M600008), National Materials Genome Project of China (2016YFB0700600) and Natural Science Foundation of Guangdong Province (2015A030310138).

Supplemental information

Supplemental Information includes 10 figures and 4 table and can be found with this article online at https://doi.org/10.1016/j.nanoen.

Declaration of interests

The authors declare no competing interests.

Appendix A. Supporting information

Supplementary data associated with this article can be found in the online version at doi:10.1016/j.nanoen.2019.02.053.

References

[1] J. Suntivich, K.J. May, H.A. Gasteiger, J.B. Goodenough, Y. Shao-Horn, A perovskite oxide optimized for oxygen evolution catalysis from molecular orbital principles, Science 334 (2011) 1383–1385.

[2] B. Zhang, X. Zheng, O. Voznyy, R. Comin, M. Bajdich, M. García-Melchor, L. Han, J. Xu, M. Liu, L. Zheng, Homogeneously dispersed multimetal oxygen-evolving catalysts, Science 352 (2016) 333–337.

[3] R.D. Smith, M.S. Prévot, R.D. Fagan, Z. Zhang, P.A. Sedach, M.K.J. Siu, S. Trudel, C.P. Berlinguette, Photochemical route for accessing amorphous metal oxide materials for water oxidation catalysis, Science (2013) 1233638.

[4] S. Zhao, Y. Wang, J. Dong, C.-T. He, H. Yin, P. An, K. Zhao, X. Zhang, C. Gao, L. Zhang, Ultrathin metal–organic framework nanosheets for electrocatalytic oxygen evolution, Nat. Energy 1 (2016) 16184.

[5] K.A. Stoerzinger, L. Qiao, M.D. Biegalski, Y. Shao-Horn, Orientation-dependent oxygen evolution activities of rutile IrO2 and RuO2, J. Phys. Chem. Lett. 5 (2014) 1636–1641.

[6] Y. Pi, N. Zhang, S. Guo, J. Guo, X. Huang, Ultrathin laminar Ir superstructure as highly efficient oxygen evolution electrocatalyst in broad pH range, Nano Lett. 16 (2016) 4424–4430.

[7] T. Shinagawa, M.T.K. Ng, K. Takanabe, Boosting the performance of the nickel anode in the oxygen evolution reaction by simple electrochemical activation, Angew. Chem. 129 (2017) 5143–5147.

[8] X.F. Lu, L.F. Gu, J.W. Wang, J.X. Wu, P.Q. Liao, G.R. Li, Bimetal-organic framework derived CoFe2O4/C porous hybrid nanorod arrays as high-performance electrocatalysts for oxygen evolution reaction, Adv. Mater. 29 (2017).

[9] T.Y. Ma, S. Dai, M. Jaroniec, S.Z. Qiao, Metal–organic framework derived hybrid Co3O4-carbon porous nanowire arrays as reversible oxygen evolution electrodes, J. Am. Chem. Soc. 136 (2014) 13925–13931.

[10] Y. Yang, L. Dang, M.J. Shearer, H. Sheng, W. Li, J. Chen, P. Xiao, Y. Zhang, R.J. Hamers, S. Jin, Highly active trimetallic NiFeCr layered double hydroxide electrocatalysts for oxygen evolution reaction, Adv. Energy Mater. (2018).

[11] W. Liu, H. Liu, L. Dang, H. Zhang, X. Wu, B. Yang, Z. Li, X. Zhang, L. Lei, S. Jin, Amorphous cobalt–iron hydroxide nanosheet electrocatalyst for efficient electrochemical and photo-electrochemical oxygen evolution, Adv. Funct. Mater. 27 (2017).

[12] H. Liang, F. Meng, M. Cabán-Acevedo, L. Li, A. Forticaux, L. Xiu, Z. Wang, S. Jin, Hydrothermal continuous flow synthesis and exfoliation of NiCo layered double hydroxide nanosheets for enhanced oxygen evolution catalysis, Nano Lett. 15 (2015) 1421–1427.

[13] J.-Q. Shen, P.-Q. Liao, D.-D. Zhou, C.-T. He, J.-X. Wu, W.-X. Zhang, J.-P. Zhang, X.-M. Chen, Modular and stepwise synthesis of a hybrid metal–organic framework for efficient electrocatalytic oxygen evolution, J. Am. Chem. Soc. 139 (2017) 1778–1781.

[14] B.Q. endonote styleLi, S.Y. Zhang, C. Tang, X. Cui, Q. Zhang, Anionic regulated NiFe (Oxy) sulfide electrocatalysts for water oxidation, Small 13 (2017).

[15] G.F. Chen, T.Y. Ma, Z.Q. Liu, N. Li, Y.Z. Su, K. Davey, S.Z. Qiao, Efficient and stable bifunctional electrocatalysts Ni/NixMy (M = P, S) for overall water splitting, Adv. Funct. Mater. 26 (2016) 3314–3323.

[16] M.-R. Gao, X. Cao, Q. Gao, Y.-F. Xu, Y.-R. Zheng, J. Jiang, S.-H. Yu, Nitrogen-doped graphene supported CoSe2 nanobelt composite catalyst for efficient water oxidation, ACS Nano 8 (2014) 3970–3978.

[17] R. Zhang, X. Wang, S. Yu, T. Wen, X. Zhu, F. Yang, X. Sun, X. Wang, W. Hu, Ternary NiCo2Px nanowires as pH-universal electrocatalysts for highly efficient hydrogen evolution reaction, Adv. Mater. 29 (2017).

[18] X. Xiao, C.-T. He, S. Zhao, J. Li, W. Lin, Z. Yuan, Q. Zhang, S. Wang, L. Dai, D. Yu, A general approach to cobalt-based homobimetallic phosphide ultrathin nanosheets for highly efficient oxygen evolution in alkaline media, Energy Environ. Sci. 10 (2017) 893–899.

[19] M. Cabán-Acevedo, M.L. Stone, J. Schmidt, J.G. Thomas, Q. Ding, H.-C. Chang, M.-L. Tsai, J.-H. He, S. Jin, Efficient hydrogen evolution catalysis using ternary pyrite-type cobalt phosphosulphide, Nat. Mater. 14 (2015) 1245.

[20] F. Meng, H. Zhong, D. Bao, J. Yan, X. Zhang, In situ coupling of strung Co4N and intertwined N–C fibers toward free-standing bifunctional cathode for robust, efficient, and flexible Zn–air batteries, J. Am. Chem. Soc. 138 (2016) 10226–10231.

[21] J.M.V. Nsanzimana, Y. Peng, Y.Y. Xu, L. Thia, C. Wang, B.Y. Xia, X. Wang, An efficient and earth-abundant oxygen-evolving electrocatalyst based on amorphous metal borides, Adv. Energy Mater. 8 (2018).

[22] D.-Y. Kuo, J.K. Kawasaki, J.N. Nelson, J. Kloppenburg, G. Hautier, K.M. Shen, D.G. Schlom, J. Suntivich, Influence of surface adsorption on the oxygen evolution reaction on IrO2 (110), J. Am. Chem. Soc. 139 (2017) 3473–3479.

[23] H. Kim, J. Park, I. Park, K. Jin, S.E. Jerng, S.H. Kim, K.T. Nam, K. Kang, Coordination tuning of cobalt phosphates towards efficient water oxidation catalyst, Nat. Commun. 6 (2015) 8253.

[24] H.-Y. Wang, S.-F. Hung, H.-Y. Chen, T.-S. Chan, H.M. Chen, B. Liu, In operando identification of geometrical-site-dependent water oxidation activity of spinel Co3O4, J. Am. Chem. Soc. 138 (2015) 36–39.

[25] J. Yang, J. Zheng, M. Xu, Z. Zhuo, W. Yang, L.-W. Wang, L. Dai, J. Lu, K. Amine, F. Pan, Short hydrogen bonds on reconstructed nanocrystal surface enhance oxygen evolution activity, ACS Catal. 8 (2017) 466–473.

[26] L. Trotochaud, S.L. Young, J.K. Ranney, S.W. Boettcher, Nickel–iron oxyhydroxide oxygen-evolution electrocatalysts: the role of intentional and incidental iron incorporation, J. Am. Chem. Soc. 136 (2014) 6744–6753.

[27] M.S. Burke, M.G. Kast, L. Trotochaud, A.M. Smith, S.W. Boettcher, Cobalt–iron (oxy) hydroxide oxygen evolution electrocatalysts: the role of structure and composition on activity, stability, and mechanism, J. Am. Chem. Soc. 137 (2015) 3638–3648.

[28] J.Y. Chen, L. Dang, H. Liang, W. Bi, J.B. Gerken, S. Jin, E.E. Alp, S.S. Stahl, Operando analysis of NiFe and Fe oxyhydroxide electrocatalysts for water oxidation: detection of Fe4+ by Mossbauer spectroscopy, J. Am. Chem. Soc. 137 (2015) 15090–15093.

[29] K. Fominykh, P. Chernev, I. Zaharieva, J. Sicklinger, G. Stefanic, M. Döblinger, A. Müller, A. Pokharel, S. Böcklein, C. Scheu, Iron-doped nickel oxide nanocrystals as highly efficient electrocatalysts for alkaline water splitting, ACS Nano 9 (2015) 5180–5188.

[30] D. Friebel, M.W. Louie, M. Bajdich, K.E. Sanwald, Y. Cai, A.M. Wise, M.-J. Cheng, D. Sokaras, T.-C. Weng, R. Alonso-Mori, Identification of highly active Fe sites in (Ni, Fe) OOH for electrocatalytic water splitting, J. Am. Chem. Soc. 137 (2015) 1305–1313.

[31] C. Tang, H.S. Wang, H.F. Wang, Q. Zhang, G.L. Tian, J.Q. Nie, F. Wei, Spatially confined hybridization of nanometer-sized nife hydroxides into nitrogen-doped graphene frameworks leading to superior oxygen evolution reactivity, Adv. Mater. 27 (2015) 4516–4522.

[32] Y. Zhu, W. Zhou, Y. Chen, J. Yu, M. Liu, Z. Shao, A high-performance electrocatalyst for oxygen evolution reaction: LiCo0.8Fe0.2O2, Adv. Mater. 27 (2015) 7150–7155.

[33] Q. Zhao, J. Yang, M. Liu, R. Wang, G. Zhang, H. Wang, H. Tang, C. Liu, Z. Mei, H. Chen, F. Pan, Tuning electronic push/pull of ni-based hydroxides to enhance hydrogen and oxygen evolution reactions for water splitting, ACS Catal. 8 (2018) 5621–5629.

[34] J. Yang, L. Hu, J. Zheng, D. He, L. Tian, S. Mu, F. Pan, Li2FeSiO4 nanorods bonded with graphene for high performance batteries, J. Mater. Chem. A 3 (2015) 9601–9608.

[35] Y. Pi, Q. Shao, P. Wang, F. Lv, S. Guo, J. Guo, X. Huang, Trimetallic oxyhydroxide coralloids for efficient oxygen evolution electrocatalysis, Angew. Chem. 129 (2017) 4573–4577.

[36] X. Han, C. Yu, S. Zhou, C. Zhao, H. Huang, J. Yang, Z. Liu, J. Zhao, J. Qiu, Ultrasensitive iron-triggered nanosized Fe-CoOOH integrated with graphene for highly efficient oxygen evolution, Adv. Energy Mater. 7 (2017).

[37] J. Liu, D. Zhu, T. Ling, A. Vasileff, S.-Z. Qiao, S-NiFe2O4 ultra-small nanoparticle built nanosheets for efficient water splitting in alkaline and neutral pH, Nano Energy 40 (2017) 264–273.

[38] T. Shinagawa, A.T. Garcia-Esparza, K. Takanabe, Insight on Tafel slopes from a microkinetic analysis of aqueous electrocatalysis for energy conversion, Sci. Rep. 5 (2015) 13801.

[39] G. Zhang, H. Wang, J. Yang, Q. Zhao, L. Yang, H. Tang, C. Liu, H. Chen, Y. Lin, F. Pan, Temperature effect on co-based catalysts in oxygen evolution reaction, Inorg. Chem. 57 (2018) 2766–2772.

[40] J. Yang, X. Kang, D. He, A. Zheng, M. Pan, S. Mu, Graphene activated 3D-hierarchical flower-like Li2FeSiO4 for high-performance lithium-ion batteries, J. Mater. Chem. A 3 (2015) 16567–16573.

[41] W. Guan, B. Pan, P. Zhou, J. Mi, D. Zhang, J. Xu, Y. Jiang, A high capacity, good safety and low cost Na2FeSiO4-based cathode for rechargeable sodium-ion battery, ACS Appl. Mater. Interfaces 9 (2017) 22369–22377.

[42] K. Du, J. Zhu, G. Hu, H. Gao, Y. Li, J.B. Goodenough, Exploring reversible oxidation of oxygen in a manganese oxide, Energy Environ. Sci. 9 (2016) 2575–2577.

[43] K. Fan, H. Chen, Y. Ji, H. Huang, P.M. Claesson, Q. Daniel, B. Philippe, H. Rensmo, F. Li, Y. Luo, Nickel–vanadium monolayer double hydroxide for efficient electrochemical water oxidation, Nat. Commun. 7 (2016) 11981.

[44] H. Liang, A.N. Gandi, D.H. Anjum, X. Wang, U. Schwingenschlögl, H.N. Alshareef, Plasma-assisted synthesis of NiCoP for efficient overall water splitting, Nano Lett. 16 (2016) 7718–7725.

[45] H. Shi, H. Liang, F. Ming, Z. Wang, Efficient overall water-splitting electrocatalysis using lepidocrocite VOOH hollow nanospheres, Angew. Chem. 129 (2017) 588–592.

[46] J. Nai, Y. Lu, L. Yu, X. Wang, X.W.D. Lou, Formation of Ni–Fe mixed diselenide nanocages as a superior oxygen evolution electrocatalyst, Adv. Mater. 29 (2017).

Jinlong Yang received his Ph.D. degree in 2014 from Wuhan University of Technology. He was a postdoctoral fellow from 2014 to 2018 at School of Advanced Materials, Peking University, Shenzhen Graduate School, China. In 2018, he joined Stanford University, USA as a postdoctoral visiting scholar, His research interests include: energy materials (battery and catalysis), nanotechnology and electrochemistry.

Prof. Yinguo Xiao received his Ph.D. degree from Institute of Physics, Chinese Academy of Sciences, China in 2006. He was a postdoctoral fellow from 2007 to 2009 and a research scientist from 2009 to 2014 at Juelich Research Center (Forschungszentrum *Jülich*), Germany. He became a tenured staff scientist in Juelich Research Center since 2015. In 2017, he joined Peking University Shenzhen Graduate School, China as an associate professor. His research interests are on development of new materials for energy conversion and storage, and characterization of complex materials using X-ray and neutron scattering techniques.

Qinghe Zhao received his B.S. degree from the School of Materials Science and Engineering at University of Science and Technology of Beijing (USTB, China) in 2010, and earned Ph.D. degree from the School of Advanced Materials at USTB in 2016, majoring in the electrochemical corrosion behavior of iron-based alloys, under the supervision of Prof. Minxu Lu. Dr. Zhao is now accepting his postdoctoral training with Prof. Feng Pan at the School of Advanced Materials, Peking University Shenzhen Graduate School, China. His research interests mainly focus on the key materials and technologies for energy storage and conversion applications, including electrocatalysts, zinc ion batteries, and sodium ion batteries.

Guangxing Zhang received his master degree in mechanics from Peking University in 2018. Then he became a research associate at School of Advanced Materials, Peking University, Shenzhen Graduate School. He is now a product manager of a LED company which provides the Mini/Micro LED product. His research interest focuses on Lithium-ion battery materials.

Rui Wang received his B.S. degree in Applied Physics from China University Of Petroleum(East China) in 2017. He is pursuing his M.S. degree in the School of Advanced Materials, Peking University, China. His research interest is energy materials.

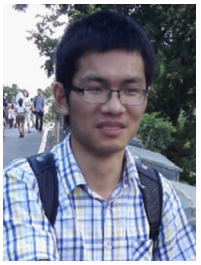

Gaofeng Teng received his master degree in mechanics from Peking University in 2017. Then he became a research associate at School of Advanced Materials, Peking University, Shenzhen Graduate School. He is now a Ph.D. student in Hong Kong. His research interest focuses on computational material.

Xin Chen is currently a postgraduate student in Prof. Feng Pan's group at the School of Advanced Materials, Peking University, Shenzhen Graduate School. He received his B.S. in School of Materials Science and Engineering, Central South University, China. His research mainly focuses on theoretical calculation and design of advanced materials.

Mouyi Weng is currently a Ph.D. candidate in Prof. Feng Pan's group at Peking University Shenzhen Graduate School, China. He received his B.S. degree from Tsinghua University in 2015. His research interests include: computational materials, materials simulation algorithms and electronic structure calculation in materials

Dr. Daping He is a full professor at Wuhan University of Technology. He obtained his Ph.D. degree in Materials Processing Engineering from Wuhan University of Technology in 2013. He was a Postdoctoral Fellow in the University of Science and Technology of China. Then he joined University of Bath as a Newton International Fellow and University of Cambridge as a Postdoctoral Fellow. His research interest is preparation and application of nano composite materials into new energy devices, sensors and RF microwaves field. He has published over 70 peer-reviewed papers and 5 Chinese patents.

Dr. Shichun Mu is currently working as a professor at Wuhan University of Technology. He received his B.S. degree from Jilin University in 1995 and Ph.D. degree from Chinese Academy of Sciences, China in 2001. Afterwards, he joined the Wuhan University of Technology as a postdoctoral researcher, 2001–2003. He has been a full professor since 2006 at Wuhan University of Technology. He was an academic visitor at Inorganic Chemistry Laboratory, University of Oxford (2007–2008). His research focuses on nanocarbon materials, PEM fuel cell catalysts, lithium ion battery materials and related devices. He has published over 200 papers and patents.

Prof. Yuan Lin, Institute of Chemistry, Chinese academy of Sciences, born in 1964, got B.S. from Dept. Chemistry, Peking University in1985, M.S. and Ph.D. from Chinese Academy of Sciences (CAS) in 1988 and 1995 respectively. In 1988–1999, he took the position of assistant professor in Institute of photographic Chemistry, Chinese academy of Sciences. From 1999 to present, he took the position of professor. For more than 20 years, Prof. Lin has been engaged in the fields of photoelectrochemical conversion of solar energy, preparation of nanocrystalline semiconductors, investigation of photoelectrochemical and surface properties of nanocrystalline semiconductors, developing ionic liquid and polymeric materials for electrolytes.

Prof. Feng Pan, National 1000-plan Professor, Founding Dean of School of Advanced Materials, Peking University Shenzhen Graduate School, Director of National Center of Electric Vehicle Power Battery and Materials for International Research, got B.S. from Dept. Chemistry, Peking University in1985 and Ph.D. from Dept. of P&A Chemistry, University of Strathclyde, Glasgow, UK, with "Patrick D. Ritchie Prize" for the best Ph.D. in 1994. With more than a decade experience in large international incorporations, Prof. Pan has been engaged in fundamental research and product development of novel optoelectronic and energy storage materials and devices. As Chief Scientist, Prof. Pan led 8 entities in Shenzhen to win the 150 million RMB grant for the national new energy vehicles (power battery) innovation project from 2013 to end of 2015. As Chief Scientist, Prof. Pan led 12 entities to win National Key project of Material Genomic Engineering for Solid State Li-ion Battery in China in 2016.